Additive Manufacturing 27 (2019) 72–79

Contents lists available at ScienceDirect

Additive Manufacturing

journal homepage: www.elsevier.com/locate/addma

Full Length Article

Binder jetting of the AlCoCrFeNi alloy

Dennis Karlsson[a,*], Greta Lindwall[b], Andreas Lundbäck[c], Mikael Amnebrink[d], Magnus Boström[d], Lars Riekehr[a], Mikael Schuisky[d], Martin Sahlberg[a], Ulf Jansson[a]

[a] Department of Chemistry – Ångström Laboratory, Uppsala University, Box 523, SE-751 20 Uppsala, Sweden
[b] Royal Institute of Technology (KTH), Department of Material Science and Engineering, Brinellvägen 23, 100 44 Stockholm, Sweden
[c] Luleå University of Technology, SE-97187 Luleå, Sweden
[d] Sandvik Additive Manufacturing, Sandvik AB, Box 510, SE-101 30 Stockholm, Sweden

ARTICLE INFO

Keywords:
Additive manufacturing
Binder jetting
High-entropy alloy
HEA

ABSTRACT

High density components of an AlCoCrFeNi alloy, often described as a high-entropy alloy, were manufactured by binder jetting followed by sintering. Thermodynamic calculations using the CALPHAD approach show that the high-entropy alloy is only stable as a single phase in a narrow temperature range below the melting point. At all other temperatures, the alloy will form a mixture of phases, including a sigma phase, which can strongly influence the mechanical properties. The phase stabilities in built AlCoCrFeNi components were investigated by comparing the as-sintered samples with the post-sintering annealed samples at temperatures between 900 °C and 1300 °C. The as-sintered material shows a dominant B2/bcc structure with additional fcc phase in the grain boundaries and sigma phase precipitating in the grain interior. Annealing experiments between 1000 °C and 1100 °C inhibit the sigma phase and only a B2/bcc phase with a fcc phase is observed. Increasing the temperature further suppresses the fcc phase in favor for the B2/bcc phases. The mechanical properties are, as expected, dependent on the annealing temperature, with the higher annealing temperature giving an increase in yield strength from 1203 MPa to 1461 MPa and fracture strength from 1996 MPa to 2272 MPa. This can be explained by a hierarchical microstructure with nano-sized precipitates at higher annealing temperatures. The results enlighten the importance of microstructure control, which can be utilized in order to tune the mechanical properties of these alloys. Furthermore, an excellent oxidation resistance was observed with oxide layers with a thickness of less than 5 µm after 20 h annealing at 1200 °C, which would be of great importance for industrial applications.

1. Introduction

High-entropy alloy (HEA) is a relatively new type of material that was reported by Cantor et al. and Yeh et al. simultaneously in 2004 [1,2]. A HEA is a solid solution of, generally, five or more elements that crystallizes in a simple bcc or fcc-like structure. The large entropy of mixing in such a multicomponent alloy is assumed to stabilize a solid solution instead of a mixture of intermetallic phases. HEAs have many interesting properties such as excellent mechanical properties at various temperatures [3], oxidation resistance [4,5], corrosion resistance [6], good hydrogen storage capabilities [7–10] and promising thermoelectric properties. Since their first discovery, a large number of alloys have been investigated. The most studied HEA is the so called Cantor alloy, CoCrFeMnNi.

The AlCoCrFeNi system has been widely studied because of the good mechanical properties in combination with a good oxidation resistance [4]. This alloy is commonly reported as a HEA, but it is well known that it forms a mixture of a CrFe-rich bcc phase (W-type) and an AlNi-rich B2 phase (CsCl-type) [4,11–13]. The alloy is also reported to decompose into both fcc (Cu-type) and sigma phases at elevated temperatures. Furthermore, spinodal decomposition into Cr-rich regions in the bcc phase has been reported for AlCoCrFeNi [11,14] and AlCoCrCuFeNi [15,16] alloys. Hence, the mechanical properties of such an alloy will depend on size, fraction and distribution of the different phases. Since the microstructure can be controlled by thermal treatments and annealing procedure this enables a tuning of the materials properties.

Additive manufacturing (AM) is an interesting method to manufacture high performance materials with complex geometries. Powder bed methods such as selective electron beam melting (SEBM) and selective laser melting (SLM) are promising techniques to produce components of high performance alloys. A problem with these techniques, however, is that the thermal treatment of the alloy during melting is

* Corresponding author.
E-mail address: dennis.karlsson@kemi.uu.se (D. Karlsson).

https://doi.org/10.1016/j.addma.2019.02.010
Received 9 January 2019; Received in revised form 18 February 2019; Accepted 19 February 2019
Available online 20 February 2019

difficult to control, which may lead to unwanted phase transformations (e.g. formation of brittle phases) during the building process. AlCoCrFeNi alloys produced by SEBM and SLM has earlier been reported [14,17]. Superior mechanical properties were observed for the SEBM samples compared to casted specimens, attributed to the finer microstructure in the AM built samples [17]. Furthermore, a fcc phase was observed in the grain boundaries, which increased the plasticity of the alloy. In contrast, it was not possible to build components of the AlCoCrFeNi alloy with a SLM process [14]. High porosity and cracks were observed, which was attributed to thermal cycling during the SLM process [14].

An alternative technique to build components of AlCoCrFeNi is powder binder jet printing. This is a fast, low-cost AM process. The powder is applied in a layer-by-layer fashion and selectively bonded using a binder. The component is then post-treated to cure the binder, followed by final sintering of the green body to a dense material [18,19]. The aim of this study was to investigate the microstructure and mechanical properties of the AlCoCrFeNi alloy produced by binder jetting followed by sintering. The expected phase composition at different temperatures has been determined by thermodynamic calculations using the CALPHAD approach. The phase composition has been correlated to the thermodynamic results, using controlled annealing experiments followed by rapid quenching.

2. Experimental procedure

Powder for AM of the AlCoCrFeNi HEA was prealloyed and gas atomized by Sandvik Osprey. The AM was performed using an ExOne X1 lab instrument by binder jetting with a powder particle size of less than 32 µm. The parameters were set to 50 µm layer thickness, recoating speed of 1 mm/s, binder saturation 60%, heating power of 50% and a drying time of 25 s (longer time was used in the beginning of the build in order to stabilize a temperature of 40 °C). After the printing process, the samples were cured at 200 °C over night followed by a sintering process using a furnace operating with a Ar/H_2 mixture to ensure a non-oxidizing atmosphere. The binder was removed by annealing at 400 °C prior to the sintering at 1320 °C for 4 h. Finally, the samples were heat treated using a furnace operated air followed by water quenching to study phase compositions. The phases were characterized by X-ray diffraction (XRD) experiments in a Bruker D8 advance equipped with a Lynxeye-XE position sensitive detector using CuK_α radiation.

Microstructure investigation was carried out by scanning electron microscopy (SEM) imaging and electron backscatter diffraction (EBSD) in a Zeiss Merlin equipped with a Nordlys Max detector for EBSD analysis and an X-Max 80 mm^2 Silicon Drift Detector for energy-dispersive X-ray spectroscopy (EDS). Aztec HKL was used for data acquisition and phase identification of EBSD patterns. The samples for microscopy were prepared by sequential polishing using 9 µm, 3 µm and 1 µm diamond particles followed by a final polishing step using 40 nm colloidal SiO_2. Furthermore, electrochemical etching using 10% Oxalic acid and a voltage of 4 V for 5 s was used prior to microstructure characterization. A FEI Titan Themis 200 (scanning) transmission electron microscope (S-TEM) with probe corrector and SuperX EDS system was used for studies of crystal structure and elemental composition of precipitates. The TEM lamella was prepared using a FEI Strata DB 235 Focused Ion Beam (FIB), using the *in-situ* lift-out technique.

An Instron 8800 testing machine with a load capability of 100 kN was employed for the compressive tests at room temperature with a true strain rate of 5×10^{-4} s^{-1}. The cylinder-shaped specimens were machined to a diameter of 6 mm and cut to a length of 8 mm using electrical discharge machining. The sharp edges were removed by polishing with 1200 grit SiC paper. The true stress is computed with the assumption of incompressibility and that the sample maintain the shape of a perfect cylinder during the entire loading cycle. The hardness measurements were performed using a load of 0.5 kgf for 15 s in a Matsuzawa MXT 50 on polished specimens.

3. Results and discussion

3.1. Thermodynamic calculations

To compare the experimental observations in the present work with the current understanding of the thermodynamics of the system, thermodynamic calculations in terms of CALPHAD (CALculations of PHAse Diagrams) were performed. In the CALPHAD approach, the thermodynamic properties of each phase of the system are described by parameterizing the Gibbs free energy as a function of composition, temperature and pressure. Multicomponent CALPHAD databases are constructed by combining descriptions of lower order systems (often up to ternaries) which then, in conjunction with extrapolation methods, can be used to calculate thermodynamic properties and phase equilibria for higher-order systems. The approach's ability to extrapolate into multicomponent space as well as into metastable regions, have proved its usefulness in computational materials design of many types of alloy systems including HEAs [20–24]. For the calculations in the present work the commercial thermodynamic database for HEA system by Thermo-Calc Software, TCHEA3, was applied [25,26].

The calculated equilibrium phase fractions for equiatomic AlCoCrFeNi as a function of temperature are shown in Fig. 1a. As can be seen, the equilibrium phase composition is complex. At low temperatures (below 300 °C), the alloy forms a mixture of a bcc and ordered bcc (B2) phases. In contrast to the bcc phase, which has two identical lattice positions (0, 0, 0) and (½, ½, ½), the B2 phase is ordered and have different elemental occupancy on the two lattice positions (see Fig. 1b and c). The compositions of the different phases are summarized in Fig. 2. As can be seen in Fig. 2a, the low temperature bcc phase (LT bcc) contains mainly of Cr with small amounts of Fe and Co in a random solid solution. The low temperature B2 (LT B2) phase, however, is more complex with Fe and Al on one lattice position and Co and Ni on the other site (Fig. 2b). It should be noted that solid lines and hatched lines for the B2 phases denote the fractional occupancy on the (0, 0, 0) and (½, ½, ½) sites, respectively. For temperatures above 300 °C, the LT B2 phase is enriched in Fe and Co with some solid solution of Cr and depleted in Ni and Al. This is at expense of forming the high temperature B2 (HT B2) phase which is enriched in Ni and Al (see Fig. 2c). As the temperature increases, the relative amount of the LT B2 and LT bcc phases decrease and is completely transformed into other phases between 450 °C and 650 °C. This is due to the formation of the HT B2 phase and a new sigma phase starting at around 300 °C and 550 °C, respectively. As expected, the sigma phase is CrFe-rich with small amounts of Co and Ni (Fig. 2d). The sigma phase is formed at the expense of the CrFe-rich LT bcc phase together with some Fe and Co from the HT B2 phase (seen as a decrease in the amount of Fe and Co around 550 °C in Fig. 2c for the HT B2 phase). In the temperature range between 675 °C and 975 °C the alloy contains of two phases, the AlNi-rich HT B2 phase and the CrFe-rich sigma phase (Fig. 1). The sigma phase becomes non-stable at higher temperatures and is completely replaced by a CrFe-rich high temperature bcc (HT bcc) phase at around 1000 °C. Above this temperature the material consists of two phases, the HT B2 phase and the HT bcc phase. There is also a minor amount of a fcc phase which is stable between 1000 °C and 1100 °C, which is rich in Cr and Fe (not shown). Finally, as can be seen in Fig. 1 the alloy has a narrow single phase region slightly below the melting point with a ordered HT B2 phase. Consequently, the CALPHAD results show that it is not correct to describe AlCoCrFeNi as a high entropy alloy from a thermodynamic point of view, except for a narrow temperature range just below the melting point.

3.2. Powder characterization

The gas atomized powder was characterized using XRD and SEM

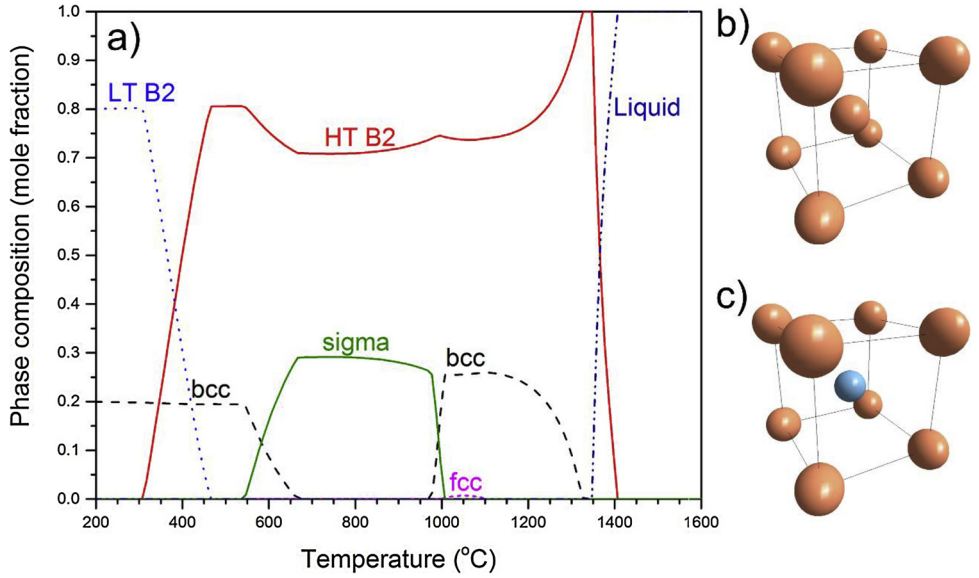

Fig. 1. a) Equilibrium phase fractions for the AlCoCrFeNi alloy, the calculation was performed using the CALPHAD method and TCHEA3 database in Thermo-Calc. b) bcc phase with random occupation of all elements on the lattice position and c) B2 phase with an ordering of the elements on the two different lattice positions.

and can be seen in Fig. 3. The diffractograms from the powder shows peaks from the bcc phase but also a peak at around $2\theta = 31^{\circ}$, originating from the (100) reflection. This peak is forbidden for the bcc structure and shows the presence of the B2 phase. It is noted that the intensities are similar to the ones for the induction melt sample, where TEM studies show presence of two phases (bcc and B2) [14]. Furthermore, the inset in Fig. 3a show the (high angle) 220 peak for the powder, where a peak splitting is seen indicating the presence of two phases (bcc and B2) with slightly different unit cell parameters. The powder morphology shows a rather large distribution of particle sizes, ranging from around 200 nm up to around 30 μm (the powder was sieved to a size below 32 μm).

3.3. Binder jetting of AlCoCrFeNi

Fig. 4a shows the as-sintered cylinder of the AlCoCrFeNi alloy prepared by binder jetting, followed by sintering at 1320 °C and cooled to room temperature in the furnace. The resulting porosity was

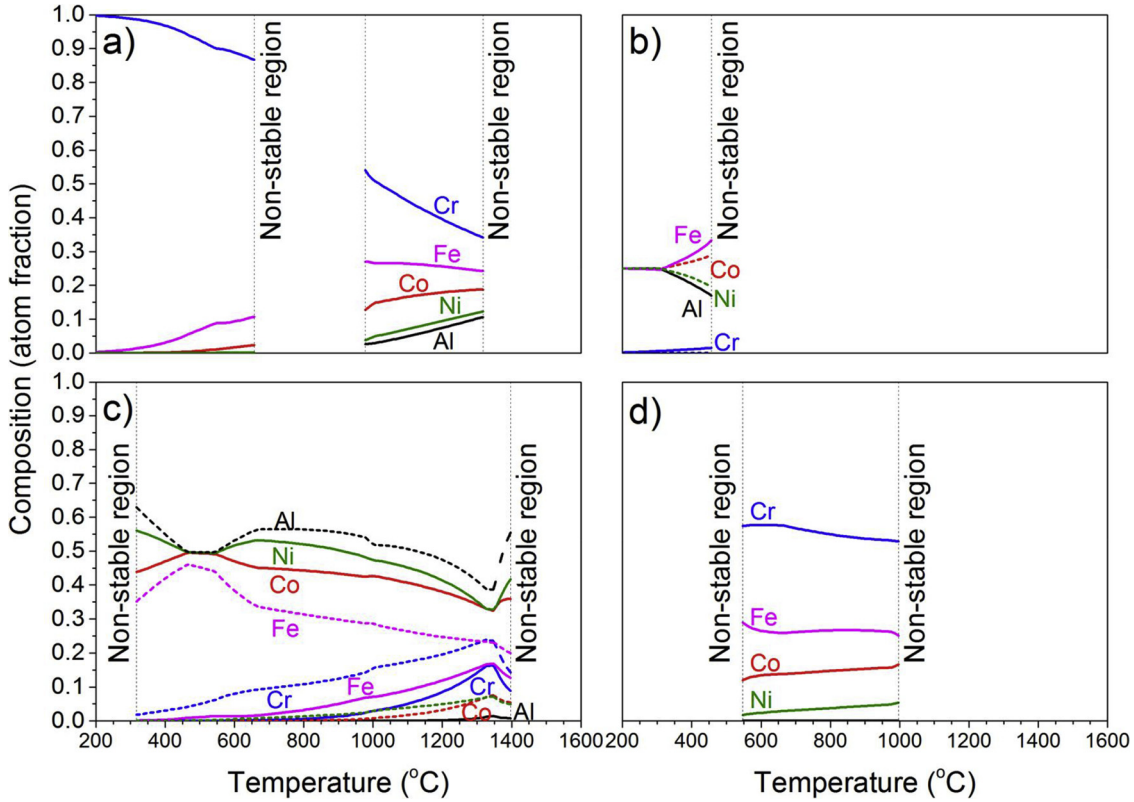

Fig. 2. Elemental composition for the a) bcc, b) LT B2, c) HT B2 and d) sigma phases in their stable regions. The dashed and solid lines for the LT and HT B2 phases indicate the atom fractions on the two different lattice positions.

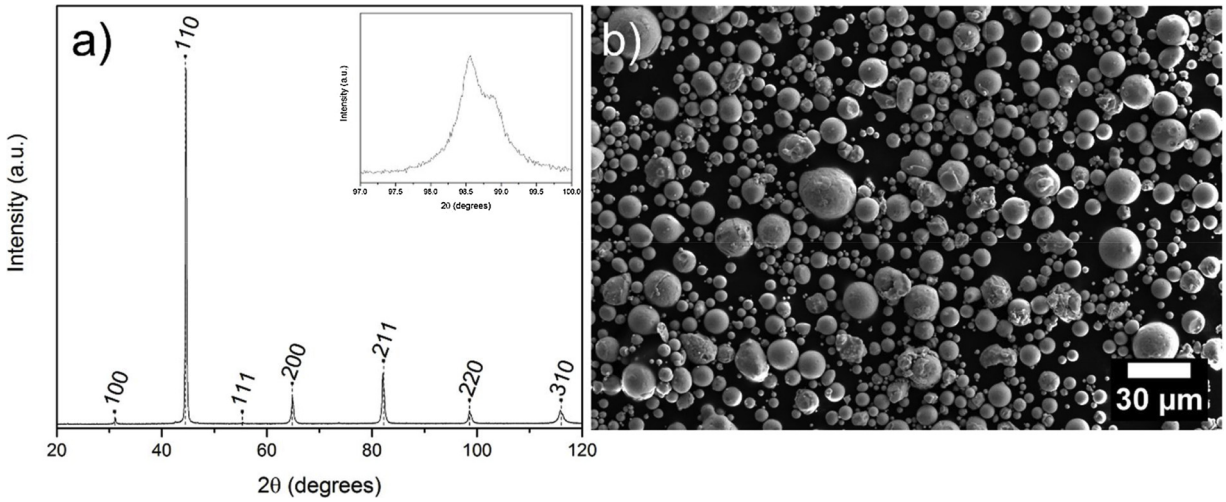

Fig. 3. Powder characterization of the gas atomized AlCoCrFeNi HEA showing a) the XRD pattern and b) SEM micrograph of the powder morphology.

estimated to around 1% from optical images of polished surfaces (the area analyzed was around 4 x 5 mm) using the ImageJ software [27]. Furthermore, the diameter and length of the samples after sintering were measured to 90% and 82%, respectively (compared to dimensions before sintering). The edges of the sample were compacted slightly more than the center (86% compared to 90%) during sintering, but further geometric design is outside the scope of this study. Upon machining the built cylinders were found to be brittle. XRD showed that the as-sintered samples consisted of a phase mixture of bcc, B2, fcc and sigma phases (Fig. 4b), in agreement with the thermodynamic calculations in Fig. 1. During the sintering step, close to the melting temperature, a mixture of bcc and B2 phases is expected. As the cooling rate of the furnace after sintering is rather slow (around 4 °C/min) significant amounts of sigma and fcc phases have time to form. The poor machinability of the alloy can be explained by the presence of the brittle sigma phase. The results show that binder jetting of AlCoCrFeNi with a standard cooling procedure cannot form components with sufficient mechanical properties due to phase formations during the cooling step in the furnace.

3.4. Post-sintering annealing of the AlCoCrFeNi alloy produced by binder jetting

The results presented above show that a brittle sigma phase is formed after the sintering step. In order to control the amount of sigma phase, a post-sintering annealing step can be applied at temperatures according to the thermodynamic modelling shown in Fig. 1 followed by rapid cooling of the component. This was demonstrated by a series of annealing temperatures in a separate furnace during 2 h at temperatures from 900 °C to 1300 °C. The experiments were conducted in air, followed by rapid quenching in water. Only up to 5 µm of oxides (Al-rich and Cr-rich) were observed after annealing up to 20 h. This shows that the AlCoCrFeNi possesses excellent high temperature oxidation resistance. The results are summarized in Fig. 5, showing diffractograms from samples annealed at five different temperatures. As can be seen, the results are in accordance to the predicted phase stability in Fig. 1. Samples quenched from 1200 °C and 1300 °C consist of a mixture of bcc and B2 phases. At 1000 °C and 1100 °C an additional fcc phase is observed, in agreement with the thermodynamic calculations. Finally, the sample annealed at 900 °C shows a mixture of bcc, B2, fcc and sigma phases. The formation of sigma phase between 800 °C to 1000 °C is in

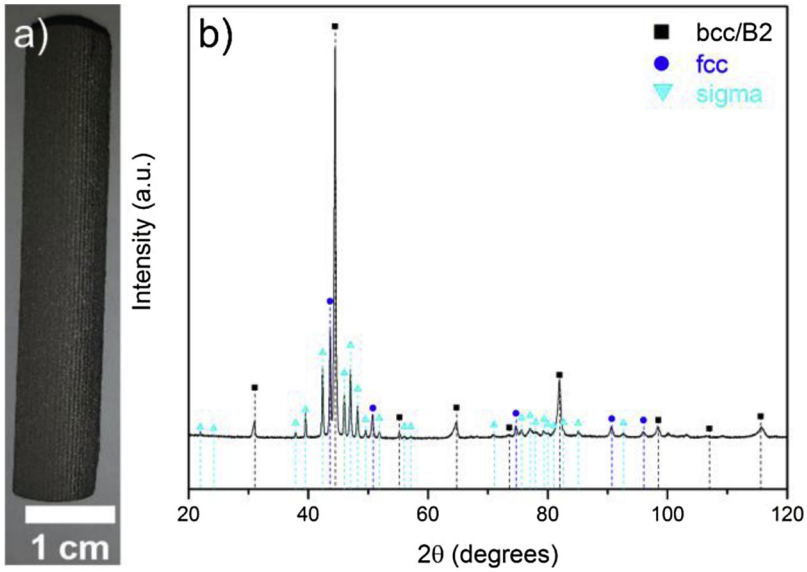

Fig. 4. a) Cylindrical sample of as-sintered AlCoCrFeNi prepared by binder jetting and sintered at 1320 °C followed by slow cooling to room temperature. b) XRD pattern of the as-sintered sample in a), showing a mixture of bcc, B2, fcc and sigma phases.

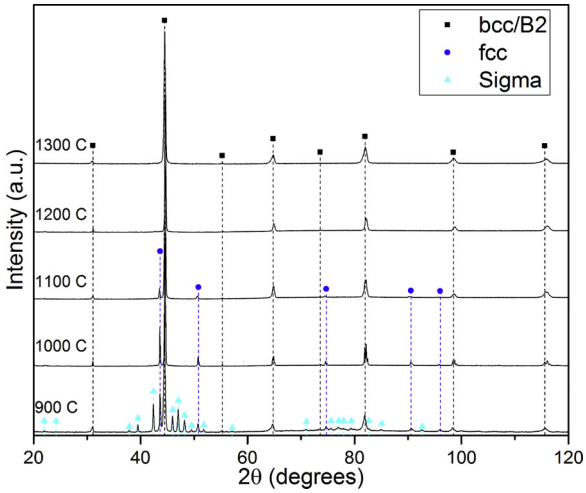

Fig. 5. a) XRD patterns of the samples annealed at temperatures from 900 °C to 1300 °C, indexed to the bcc/B2, fcc and sigma phases marked with black squares, blue circles and teal triangles (For interpretation of the references to colour in this figure legend, the reader is referred to the web version of this article).

good agreement with the thermodynamic calculations shown in Fig. 1.

Fig. 6a–c show SEM micrographs of etched samples after annealing and quenching, EBSD images of the corresponding samples are shown in Fig. 6d–f. The blue, green and yellow colors in the EBSD images represent the bcc/B2, fcc and sigma phases, respectively. Note that EBSD cannot accurately distinguish between the bcc and B2 phases. As can be seen in the SEM images, some areas have been more strongly etched than other regions. Oxalic acid was used to etch the CrFe-rich phase, strongly enhancing the contrast. According to the XRD results in Fig. 4b, the as-sintered sample should consist of a phase mixture of bcc/B2, fcc and sigma phases. The EBSD image of the as-sintered sample (Fig. 6d) shows bcc/B2 grains with the fcc phase precipitated at the grain boundaries. Furthermore, the sigma phase could be observed as precipitates within the grains. The phase fractions, extracted from the EBSD data, is 61.6%, 25.5% and 12.9% for the bcc/B2, sigma and fcc phases, respectively. The SEM image of this sample (Fig. 6a) shows a strong etching in the region corresponding to the fcc and sigma phases, which both are enriched in Fe and Cr according to the thermodynamic calculations. Post-sintering annealing and quenching from 1000 °C should according to the thermodynamic calculations and the XRD results in Fig. 5 give a phase mixture of bcc/B2 and fcc. These phases can clearly be observed in the EBSD image (Fig. 6e) and the etched microstructure in SEM (Fig. 6b). The sigma phase in the interior of the bcc/B2 grains has disappeared, while substantial amounts of fcc phase (14.9%) still is present at the grain boundaries. An interesting observation is that the bcc/B2 grains exhibit an interior etch pattern with rectangular features, which are more strongly etched than the surrounding matrix. Since the oxalic acid strongly etches Fe/Cr-rich phases, it is suggested that the etched features inside the grains consists of the CrFe-rich bcc phase, while the less etched parts of the grains consist of AlNi-rich B2 phase. Finally, after annealing at 1200 °C, the quenched sample consists of more or less only bcc/B2 phase (99.5%) with only trace amount of fcc (0.5%) observed. Fig. 6f shows the EBSD phase map, with a phase identification of the bcc/B2 phase. This is also in agreement with the thermodynamic calculations (Fig. 1). SEM of the etched sample (Fig. 6c) shows, also in this case, more strongly etched bcc regions at the grain boundaries and inside the B2 grain matrix.

An interesting observation is that higher magnifications in SEM of the samples annealed at 1200 °C after sintering show even smaller features inside the bcc and B2 grains (see inset in Fig. 6c). To study these smaller features, a TEM sample was prepared from the specimen annealed at 1200 °C. Fig. 7a shows a TEM dark field (DF) micrograph of a region between two subgrains of the bcc and B2 phases. Consequently, the top region of Fig. 7a is a bcc grain (Grain 1), while the bottom part in Fig. 7a shows a B2 grain (Grain 2). Note that the TEM analysis was made on an un-etched sample. The image is formed using the 300 reflection (forbidden reflection for the bcc phase), resulting in contrast between the two phases, where the B2 phase is excited in contrast to the bcc phase. As can be seen in Fig. 7, there is a precipitation of an AlNi-rich B2 phase (bright) in the CrFe-rich bcc phase (dark). The precipitation occurs on two different length scales, around 10–20 nm and around 100–300 nm. Similarly, precipitation of a CrFe-rich bcc phase can be seen within the AlNi-rich B2 phase. Furthermore, it can be seen that the precipitation density decreases close to the interface between grain 1 and 2 where almost no precipitates are observed. This interface layer with close to none precipitates would lower the strength of the material as dislocation movement during deformation is not blocked by precipitates, making the material softer and

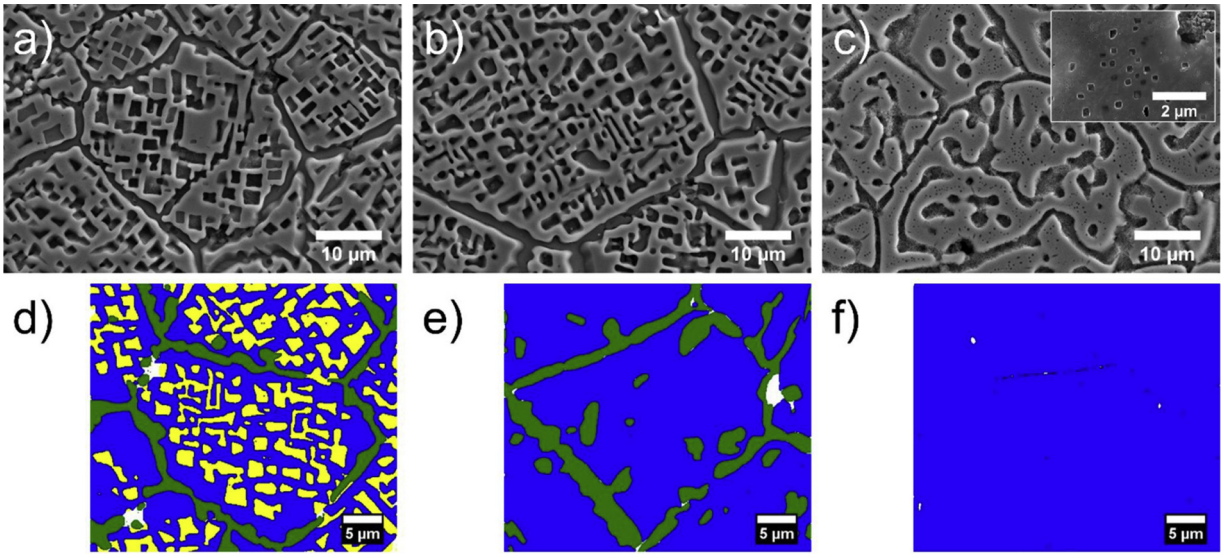

Fig. 6. a–c) shows SEM micrographs of the as-sintered sample and the samples annealed at 1000 °C and 1200 °C, respectively. The EBSD phase maps are shown e–f, with the blue, green and yellow colours representing the bcc/B2, fcc and sigma phases, respectively (For interpretation of the references to colour in this figure legend, the reader is referred to the web version of this article).

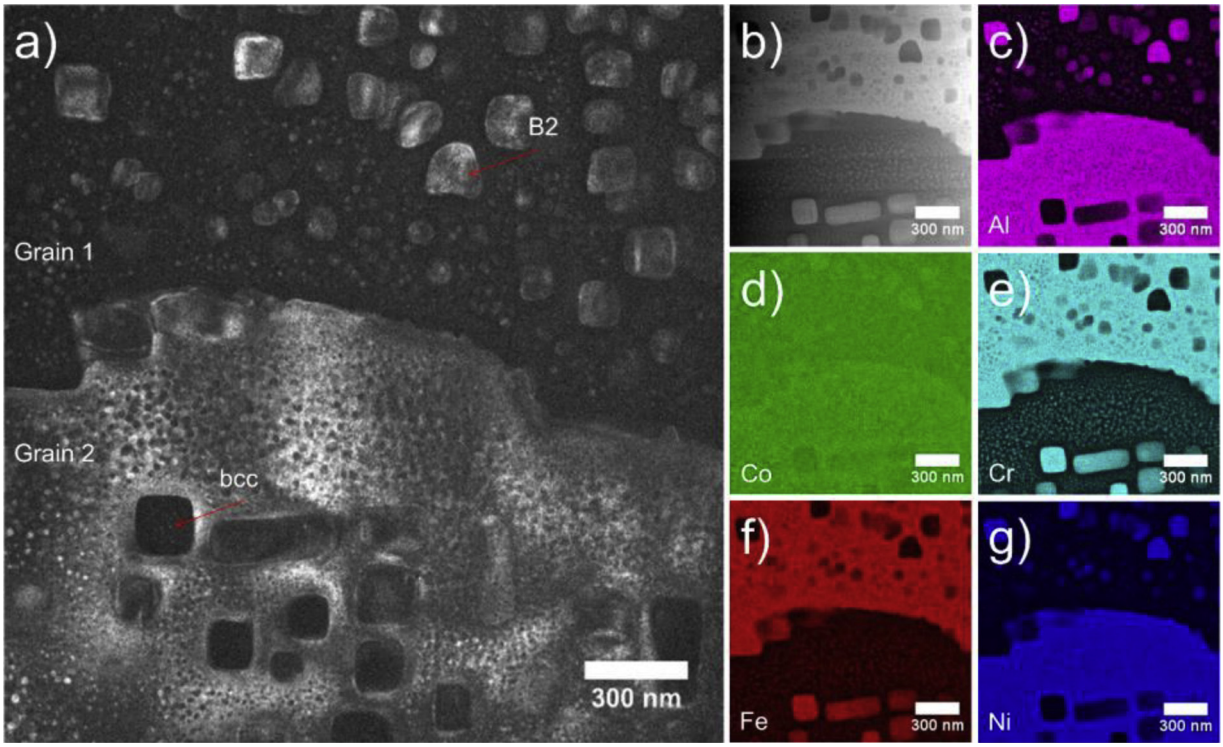

Fig. 7. Microstructure of the binder jet produced HEA after annealing at 1200 °C. a) shows a DF image using the 300 reflection in the boundary between the bcc and B2 phase within one grain, b) an high angle annular dark field (HAADF) image and c–g) elemental maps of Al, Co, Cr, Fe and Ni, respectively.

causing failure within these regions.

The results in Figs. 6 and 7 show that the samples sintered at high temperatures form an hierarchical microstructure with bcc and B2 precipitates on several different length scales. Similar microstructures has earlier been reported for the AlCoCrFeNi alloy produced using conventional methods, with a CrFe-rich bcc phase precipitating in an AlNi-rich matrix [14].The formation of such an hierarchical microstructure will be of great importance for the mechanical properties and if controlled properly opens up the possibility to tune materials properties.

3.5. Mechanical properties

The compressive stress-strain curves after annealing for 2 h at 1000 °C and 1200 °C can be seen in Fig. 8 and the corresponding yield strength (σ_y), fracture strength (σ_f) and fracture elongation (ε_f) are summarized in Table 1. The mechanical properties of the as-sintered material are not displayed, as the machinability of this alloy is extremely poor, making it impossible to achieve samples for compressive

Table 1
Summary of compressive mechanical properties; yield stress, σ_y, fracture stress, σ_f, fracture strain, ε_f at room temperature.

Annealing temp. (°C)	σ_y (MPa)	σ_f (MPa)	ε_f (%)
1000	1203 ± 22	1996 ± 45	32.25 ± 2.5
1200	1461 ± 23	2272 ± 48	31.46 ± 2.1
SEBM (0°) [17]	1015 ± 53	1668 ± 72	26.4 ± 6.7

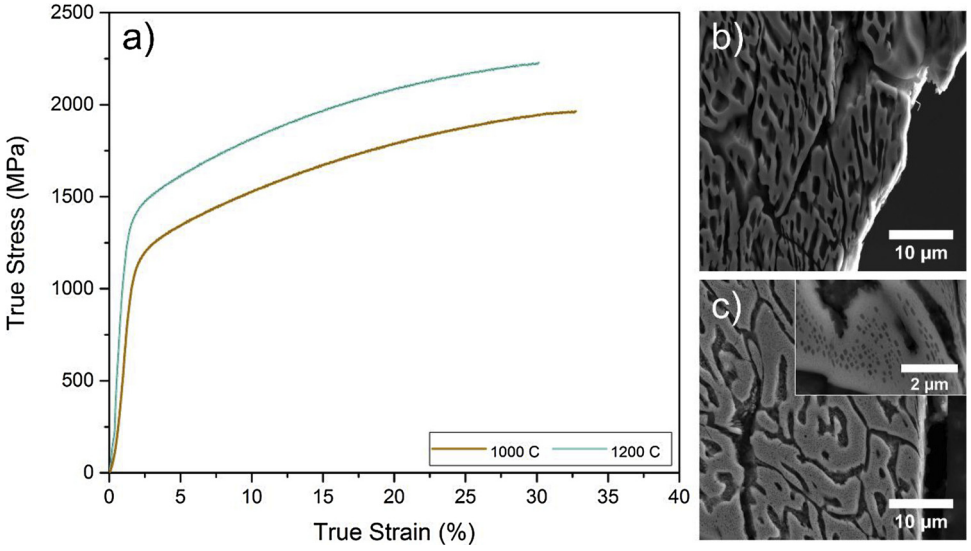

Fig. 8. a) Compressive stress-strain curves at room temperature for the samples produced by binder jetting followed by annealing at 1000 °C and 1200 °C and quenching. b) crossection of the sample annealed at 1000 °C after failure. c) crossection of the sample annealed at 1200 °C after failure and an inset showing precipitates.

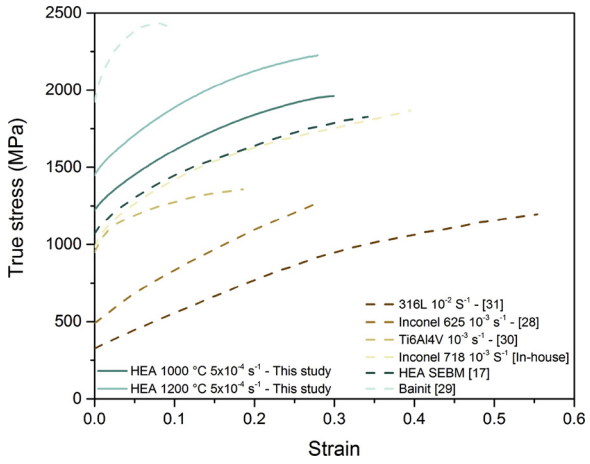

Fig. 9. Comparison of stress-strain curves at room temperature for the AlCoCrFeNi alloys produced in the current study and some selected common alloys.

tests. This is attributed to the formation of a brittle sigma phase (see Figs. 1 and 4) during the processing. However, annealing the binder jet produced samples at 1000 °C and 1200 °C produced materials with excellent properties. Fujieda et al. reported superior mechanical properties for the AlCoCrFeNi alloy produced by SEBM in comparison to casted samples of the same material [17]. Furthermore, the fracture strength for the SEBM produced AlCoCrFeNi alloy was six times higher than that of the SUS304 stainless steel. In contrast, the AlCoCrFeNi HEA produced by binder jetting followed by annealing showed a fracture strength of up to 2272 MPa, which is 60% higher than the SEBM produced material [17]. The yield strength for the binder jet produced sample after annealing at 1200 °C is higher than the one annealed at 1000 °C. This can be explained by the absence of a fcc phase in the sample after annealing at 1200 °C. Furthermore, the fracture strength and fracture elongation are higher for the sample annealed at 1200 °C compared to the sample annealed at 1000 °C. Fig. 8b and c show a crossection of the fracture after compression tests of the samples annealed at 1000 °C and 1200 °C, respectively. The samples were etched in oxalic acid to remove the CrFe-rich phase and enhance the contrast. For the sample annealed at 1000 °C (shown in Fig. 8b) a CrFe-rich phase is observed in the grain boundaries (fcc phase, see Fig. 6e) and as precipitates in the grain interior (bcc phase, see Fig. 6e). A severe plastic deformation, especially close to the fracture surface, and a transgranular failure can be observed. An intergranular failure has earlier been reported for the SEBM produced AlCoCrFeNi HEA, explained by microcracks and an elastic incompatibility of the adjacent phases. As no cracks have been observed (with the exception of some residual porosity) in the grain boundaries of the binder jet produced material, this effect is negated. Furthermore, some fcc phase is observed in the grain interiors for these samples, suggesting that an elastic incompatibility can occur in the grain interior causing a transgranular failure. For the sample annealed at 1200 °C (shown in Fig. 8c) the microstructure is very different, with a CrFe-rich phase in the grain boundaries and a large network of the two different phases (bcc and B2, see Fig. 6f) in the grain interior. Smaller precipitates (nano-scaled, described further in Fig. 7) are observed within the AlNi-rich phase, which could explain the excellent mechanical properties compared to the SEBM produced material. Also, for this sample a transgranular fracture was observed, explained by the absence of cracks in the grain boundaries and no present fcc phase (causing no/low elastic incompatibility between phases).

Fig. 9 show stress-strain curves for the materials in the present study in comparison to some well known materials [17,28–31]. It can be seen that the AlCoCrFeNi alloy has a potential to achieve high yield strength, fracture strength and fracture elongations. Additional post-sintering treatments are, however, needed to obtain desired microstructures and phase compositions. The yield strength is higher than conventional alloys like Ni-based Inconel 718 and 625, as well as $TiAl_6V_4$ and 316 L. The mechanical properties are in the range between the austenitic 316 L and the very hard bainite (which consists of cementite and ferrite phases) with high yield and fracture strength. However, the binder jet produced AlCoCrFeNi achieves high yield and fracture strength in combination with a high fracture elongation compared to bainite, which show rather low fracture elongation.

Additionally, the hardnesses (HV) were measured to 5.2(2) GPa, 4.1(1) GPa and 4.9(2) GPa or the as-sintered sample and after annealing at 1000 °C and 1200 °C, respectively. In the as-sintered sample a hard sigma phase is present, contributing to the highest measured hardness. Upon annealing the sigma phase is transformed into a fcc phase, which shows a significantly lower hardness. Further annealing dissolves the fcc phase and only a combination of bcc and b2 is observed, which shows a higher hardness compared to the sample annealed at 1000 °C (but no significant difference from the as-sintered sample). This is in agreement with the lower yield strength (and hardness) for the sample annealed at 1000 °C compared to 1200 °C.

4. Conclusions

Binder jetting was used to successfully synthesize AlCoCrFeNi with a porosity of around 1%. After sintering the alloy shows a combination of bcc, b2, fcc and sigma phases. Computational thermodynamics was used to predict phase compositions and a series of annealing experiments were conducted to confirm the phase composition and evaluate the mechanical properties. It can be seen that the phase diagram of the alloy is complex and that a single phase HEA in the AlCoCrFeNi equiatomic system is only obtained at a temperature interval close to the melting point. Annealing experiments are in agreement with the thermodynamic calculations, showing a combination of fcc and bcc/B2 phases at 1000 °C and only bcc/B2 phases at temperatures above 1200 °C. The mechanical properties are enhanced by the higher annealing temperatures, correlated to the finer microstructure and lower elastic incompatibility between phases. Furthermore, the presence of nm-scale precipitates can be beneficial for dislocation movement, further improving the mechanical properties. The comparison of the flow stress between the AlCoCrFeNi alloy and some conventional alloys shown in Fig. 9 shows that the AlCoCrFeNi alloy has a potential to achieve high yield strength, fracture strength combined with good ductility.

This study enlightens the importance of understanding the microstructure of HEAs produced by AM, or other manufacturing pathways, in order to achieve high quality materials with excellent mechanical properties. The mechanical properties can be tuned using annealing experiments, changing the constituent phases and microstructure.

Acknowledgements

Financial support from the Swedish Foundation for Strategic Research, project “SSF–Development of processes and Materials in AM”, Reference No. GMT14-0048, is greatly acknowledged.

References

[1] B. Cantor, I.T.H. Chang, P. Knight, A.J.B. Vincent, Microstructural development in equiatomic multicomponent alloys, Mater. Sci. Eng. a-Struct. 375 (2004) 213–218.
[2] J.W. Yeh, S.K. Chen, S.J. Lin, J.Y. Gan, T.S. Chin, T.T. Shun, C.H. Tsau, S.Y. Chang, Nanostructured high-entropy alloys with multiple principal elements: novel alloy design concepts and outcomes, Adv. Eng. Mater. 6 (5) (2004) 299–303.
[3] B. Gludovatz, A. Hohenwarter, D. Catoor, E.H. Chang, E.P. George, R.O. Ritchie, A fracture-resistant high-entropy alloy for cryogenic applications, Science 345 (6201) (2014) 1153–1158.
[4] T.M. Butler, M.L. Weaver, Oxidation behavior of arc melted AlCoCrFeNi multi-component high-entropy alloys, J. Alloys. Compd. 674 (2016) 229–244.
[5] G. Laplanche, U.F. Volkert, G. Eggeler, E.P. George, Oxidation behavior of the CrMnFeCoNi high-entropy alloy, Oxid. Met. 85 (5-6) (2016) 629–645.

[6] T. Fujieda, H. Shiratori, K. Kuwabara, M. Hirota, K.-T. Letters, CoCrFeNiTi-based high-entropy alloy with superior tensile strength and corrosion resistance achieved by a combination of additive manufacturing using selective electron beam melting and solution treatment, Mater. Lett. (2017).
[7] M. Sahlberg, D. Karlsson, C. Zlotea, U. Jansson, Superior hydrogen storage in high entropy alloys, Sci. Rep. 6 (2016) 36770.
[8] D. Karlsson, G. Ek, J. Cedervall, C. Zlotea, K.T. Moller, T.C. Hansen, J. Bednarcik, M. Paskevicius, M.H. Sorby, T.R. Jensen, U. Jansson, M. Sahlberg, Structure and hydrogenation properties of a HfNbTiVZr high-entropy alloy, Inorg. Chem. 57 (4) (2018) 2103–2110.
[9] I. Kunce, M. Polanski, J. Bystrzycki, Microstructure and hydrogen storage properties of a TiZrNbMoV high entropy alloy synthesized using Laser Engineered Net shaping (LENS), Int. J. Hydrogen Energy 39 (18) (2014) 9904–9910.
[10] I. Kunce, M. Polanski, J. Bystrzycki, Structure and hydrogen storage properties of a high entropy ZrTiVCrFeNi alloy synthesized using Laser Engineered Net shaping (LENS), Int. J. Hydrogen Energy 38 (27) (2013) 12180–12189.
[11] W.R. Wang, W.L. Wang, S.C. Wang, Y.C. Tsai, C.H. Lai, J.W. Yeh, Effects of Al addition on the microstructure and mechanical property of AlxCoCrFeNi high-entropy alloys, Intermetallics 26 (2012) 44–51.
[12] A. Manzoni, H. Daoud, R. Volkl, U. Glatzel, N. Wanderka, Phase separation in equiatomic AlCoCrFeNi high-entropy alloy, Ultramicroscopy 132 (2013) 212–215.
[13] A. Munitz, S. Salhov, S. Hayun, N. Frage, Heat treatment impacts the micro-structure and mechanical properties of AlCoCrFeNi high entropy alloy, J. Alloys. Compd. 683 (2016) 221–230.
[14] D. Karlsson, A. Marshal, F. Johansson, M. Schuisky, M. Sahlberg, J.M. Schneider, U. Jansson, Elemental segregation in an AlCoCrFeNi high-entropy alloy – a comparison between selective laser melting and induction melting, J. Alloys. Compd. (2018).
[15] S. Singh, N. Wanderka, B.S. Murty, U. Glatzel, J. Banhart, Decomposition in multi-component AlCoCrCuFeNi high-entropy alloy, Acta Mater. 59 (1) (2011) 182–190.
[16] S. Singh, N. Wanderka, K. Kiefer, K. Siemensmeyer, J. Banhart, Effect of decomposition of the Cr-Fe-Co rich phase of AlCoCrCuFeNi high entropy alloy on magnetic properties, Ultramicroscopy 111 (6) (2011) 619–622.
[17] T. Fujieda, H. Shiratori, K. Kuwabara, T. Kato, K. Yamanaka, Y. Koizumi, A. Chiba, First demonstration of promising selective electron beam melting method for utilizing high-entropy alloys as engineering materials, Mater. Lett. 159 (2015) 12–15.
[18] P.K. Gokuldoss, S. Kolla, J. Eckert, Additive manufacturing processes: selective laser melting, Electron beam melting and binder jetting-selection guidelines, Materials (Basel) 10 (6) (2017).
[19] P. Nandwana, A.M. Elliott, D. Siddel, A. Merriman, W.H. Peter, S.S. Babu, Powder bed binder jet 3D printing of Inconel 718: densification, microstructural evolution and challenges, Curr. Opin. Solid State Mater. Sci. 21 (4) (2017) 207–218.
[20] D.B. Miracle, J.D. Miller, O.N. Senkov, C. Woodward, M.D. Uchic, J. Tiley, Exploration and development of high entropy alloys for structural applications, Entropy 16 (1) (2014) 494–525.
[21] D.B. Miracle, O.N. Senkov, A critical review of high entropy alloys and related concepts, Acta Mater. 122 (2017) 448–511.
[22] H.L. Chen, H.H. Mao, Q. Chen, Database development and Calphad calculations for high entropy alloys: challenges, strategies, and tips, Mater. Chem. Phys. 210 (2018) 279–290.
[23] Y.H. Zhao, Y.S. Yang, C.H. Lee, W. Xiong, Investigation on phase stability of AlxCo0.2Cr0.2Ni0.2Ti0.4-x high entropy alloys, J. Phase Equilibria Diffus. 39 (5) (2018) 610–622.
[24] M. Widom, Modeling the structure and thermodynamics of high-entropy alloys, J. Mater. Res. 33 (19) (2018) 2881–2898.
[25] J.O. Andersson, T. Helander, L.H. Hoglund, P.F. Shi, B. Sundman, THERMO-CALC & DICTRA, computational tools for materials science, Calphad-Comput. Coupl. Phase Diagr. Thermochem. 26 (2) (2002) 273–312.
[26] Thermo-Calc Software, TCHEA3: TCS High Entropy Alloy Database, (2018) Available at:http://www.thermocalc.com/media/35873/tchea3_extended_info.pdf (Accessed: 17th, August 2018).
[27] C.A. Schneider, W.S. Rasband, K.W. Eliceiri, NIH Image to ImageJ: 25 years of image analysis, Nat. Methods 9 (7) (2012) 671–675.
[28] L. Suave, D. Bertheau, J. Cormier, P. Villechaise, A. Soula, Z. Hervier, F. Hamon, J. Laigo, F. Futuroscope-Chasseneuil, F. Gonfreville-LOrcher, Impact of thermo-mechanical aging on alloy 625 high temperature mechanical properties, Impact of thermomechanical aging on alloy 625 high temperature mechanical properties, John Wiley & Sons, 2014, p. 317.
[29] F.G. Caballero, H.K.D.H. Bhadeshia, K.J.A. Mawella, D.G. Jones, P. Brown, Very strong low temperature bainite, Mater. Sci. Technol. 18 (3) (2002) 279–284.
[30] B. Babu, L.E. Lindgren, Dislocation density based model for plastic deformation and globularization of Ti-6Al-4V, Int. J. Plast. 50 (2013) 94–108.
[31] L.E. Lindgren, Q. Hao, D. Wedberg, Improved and simplified dislocation density based plasticity model for AISI 316 L, Mech. Mater. 108 (2017) 68–76.